

HI-TO-H₂ TRANSITIONS IN THE PERSEUS MOLECULAR CLOUD

SHMUEL BIALY*¹, AMIEL STERNBERG¹, MIN-YOUNG LEE², FRANCK LE PETIT³ AND EVELYNE ROUEFF³

Accepted for publication in the Astrophysical Journal

ABSTRACT

We use the Sternberg et al. (2014) theory for interstellar atomic to molecular hydrogen (HI-to-H₂) conversion to analyze HI-to-H₂ transitions in five (low-mass) star-forming and dark regions in the Perseus molecular cloud, B1, B1E, B5, IC348, and NGC1333. The observed HI mass surface densities of 6.3 to 9.2 M_⊙ pc⁻² are consistent with HI-to-H₂ transitions dominated by HI-dust shielding in predominantly atomic envelopes. For each source, we constrain the dimensionless parameter αG , and the ratio I_{UV}/n , of the FUV intensity to hydrogen gas density. We find αG values from 5.0 to 26.1, implying characteristic atomic hydrogen densities 11.8 to 1.8 cm⁻³, for $I_{\text{UV}} \approx 1$ appropriate for Perseus. Our analysis implies that the dusty HI shielding layers are probably multiphased, with thermally unstable UNM gas in addition to cold CNM within the 21 cm kinematic radius.

Subject headings: ISM:individual objects (Perseus) – ISM:clouds – photon dominated regions (PDR) – galaxies:star formation

1. INTRODUCTION

Conversion of hydrogen gas from atomic (HI) to molecular (H₂) form is of critical importance for the evolution of the interstellar medium (ISM) and for star-formation in galaxies (Sternberg et al. 2014, hereafter S14).

Recently, Lee et al. (2012) and Lee et al. (2015, hereafter L12/L15) analyzed HI-to-H₂ transitions in several subregions within the well-studied Perseus molecular cloud. The Perseus cloud is itself part of the nearby Taurus-Auriga-Perseus complex located at a distance of ~ 300 pc and is embedded within the Per OB2 HI supershell (Bally et al. 2008). The Perseus cloud mass is a few 10⁴ M_⊙, and this includes the HI plus H₂ (Bachiller & Cernicharo 1986; Kirk et al. 2006). The cloud consists of an extended dusty HI envelope surrounding several condensations of dense H₂ gas (Sancisi et al. 1974; Sargent 1979; Ungerechts & Thaddeus 1987; Ridge et al. 2006). The overall angular size depends on the tracers used, and a characteristic diameter based on 21 cm kinematics is ~ 80 pc (Imara & Blitz 2011).

L12/L15 used the HI data provided by the Galactic Arecibo L-band Feed Array HI Survey (GALFA-HI survey; Peek et al. 2011), together with far-infrared data from the Improved Reprocessing of the IRAS Survey (IRIS; Miville-Deschênes & Lagache 2005) and the V-band extinction image provided by the COMPLETE Survey (Ridge et al. 2006), to derive HI and H₂ surface densities (Σ_{HI} and Σ_{H_2}) on ~ 0.4 pc scales, for several hundred sight-lines towards five dark and (low-mass) star-forming regions within Perseus. These are B1, B1E, B5 (dark), IC348, and NGC1333 (star-forming). Here we consider the data presented by L15 for which the inferred HI column densities are corrected for (small, up to 20%) 21 cm optical depth effects.

L12/L15 analyzed the Perseus data using the formalism presented by Krumholz et al. (2009, hereafter KMT) for interstellar HI-to-H₂ transitions in optically thick media. In

this paper we use the simpler and more general theory presented by S14 to reanalyze the Perseus observations. In § 1, we briefly summarize the relevant S14 formalism. In § 2 we present and fit the L15 observations of the $\Sigma_{\text{H}_2}/\Sigma_{\text{HI}}$ ratios in Perseus. In § 3 we use the observed maximal HI mass surface densities towards each H₂ cloud to constrain the controlling dimensionless parameter αG and the characteristic HI gas densities in the atomic envelopes. The observed HI mass surface densities are consistent with HI-to-H₂ transitions dominated by HI-dust shielding. The relatively low gas densities we infer suggests that the HI shielding layers are probably multiphased and are not pure CNM.

2. THEORY

2.1. HI Column Density

S14 presented a general analytic formula for the steady state column density of photodissociated HI gas in optically thick clouds illuminated by FUV radiation, derived for planar geometry and uniform density gas. For irradiation by isotropic fields, the *total* HI column density is given by

$$N_{\text{HI}} = 2 \times \frac{\langle \mu \rangle}{\sigma_g} \ln \left[\frac{1}{\langle \mu \rangle} \frac{\alpha G}{4} + 1 \right]. \quad (1)$$

In this expression, the factor of two is for two-sided illumination, $\langle \mu \rangle = 0.8$ is a geometrical factor for isotropic radiation, σ_g is the dust-grain absorption cross section per hydrogen nucleon for 912-1108 Å Lyman-Werner (LW) band radiation, and αG is the basic dimensionless parameter. As in S14 we assume that

$$\sigma_g = 1.9 \times 10^{-21} \phi_g Z'_g \text{ cm}^2, \quad (2)$$

where Z'_g is the grain abundance relative to standard Galactic ISM grain abundances. Thus, Z'_g is the “dust-metallicity”. In Equation (2) ϕ_g is a factor of order unity depending on the specific grain composition, and the scattering and absorption properties. The dimensionless parameter

$$\alpha G \equiv \frac{D_0 G}{Rn} = \bar{f}_{\text{diss}} \frac{\sigma_g w F_0}{Rn}, \quad (3)$$

¹ Raymond and Beverly Sackler School of Physics & Astronomy, Tel Aviv University, Ramat Aviv 69978, Israel

² Laboratoire AIM, CEA/IRFU/Service d’Astrophysique, Bat 709, 91191 Gif-sur-Yvette, France

³ LERMA, Observatoire de Paris, PSL Research University, CNRS, UMR8112, F-92190 Meudon, France

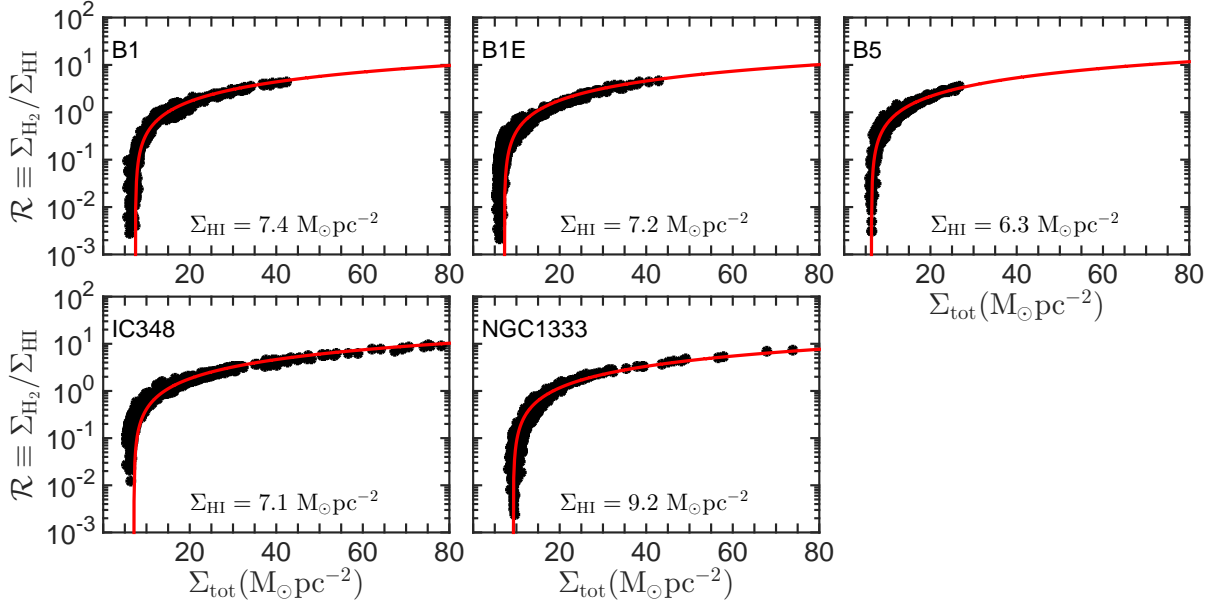


FIG. 1.— $\mathcal{R}_{\text{H}_2} \equiv \Sigma_{\text{H}_2}/\Sigma_{\text{HI}}$ as a function of $\Sigma_{\text{tot}} \equiv \Sigma_{\text{HI}} + \Sigma_{\text{H}_2}$ for the five regions: B1, B1E, B5, IC348 and NGC1333. The red curves are the “best-fits” to the data. The median errors (not displayed) are $\pm 15\%$ and $\pm 35\%$ in Σ_{tot} and \mathcal{R}_{H_2} respectively. The best-fitting values of Σ_{HI} are also indicated.

TABLE 1
TOTAL HI SURFACE DENSITIES.

Cloud	$\Sigma_{\text{HI}} (M_{\odot} \text{pc}^{-2})$	$N_{\text{HI}} (10^{20} \text{cm}^{-2})$
B1	7.4	9.3
B1E	7.2	9.0
B5	6.3	7.9
IC348	7.1	8.9
NGC1333	9.2	11.6

where D_0 is the free-space H_2 dissociation rate (s^{-1}), G is the average H_2 self-shielding factor, R is the H_2 formation rate coefficient ($\text{cm}^3 \text{s}^{-1}$), n is the total hydrogen gas density (cm^{-3}), $\bar{f}_{\text{diss}} = 0.12$ is the mean dissociation probability per H_2 -absorbed LW band photon, F_0 is the free-space LW photon flux ($\text{cm}^{-2} \text{s}^{-1}$), and $w \equiv 1/[1 + (2.64\phi_g Z'_g)^{1/2}]$ is the normalized H_2 -dust-limited dissociation bandwidth (see S14 for a detailed discussion of all these quantities). Physically, αG is the ratio of the HI-dust absorption rate of the effective unattenuated H_2 dissociation flux, to the H_2 formation rate.

For H_2 formation on dust grains $R = 3 \times 10^{-17} Z'_g \text{cm}^3 \text{s}^{-1}$, and the dimensionless parameter αG can be expressed as

$$\alpha G \equiv 1.54 \frac{I_{\text{UV}}}{n/100 \text{cm}^{-3}} \frac{\phi_g}{1 + (2.64\phi_g Z'_g)^{1/2}}, \quad (4)$$

where I_{UV} is the field intensity relative to the mean Draine (1978) interstellar field, such that $F_0 = 2.07 \times 10^7 I_{\text{UV}} \text{cm}^{-2} \text{s}^{-1}$ and $D_0 = 5.8 \times 10^{-11} I_{\text{UV}} \text{s}^{-1}$. The value of αG determines the nature of the HI-to- H_2 transition and the size of the integrated HI column. In the “weak-field” limit $\alpha G \ll 1$, N_{HI} is small, and the HI-to- H_2 transition is controlled by H_2 -line and H_2 -dust absorption. In the “strong-field” limit $\alpha G \gg 1$, N_{HI} is large, and the HI-to- H_2 transition is dominated by HI-dust absorption. Importantly, for optically thick clouds the total HI column density, N_{HI} , depends only on αG and σ_g .

2.2. Time-Scale

Equation (1) for the HI column density is for steady-state conditions such that the local H_2 destruction rate equals the formation rate, at every location. The equilibrium time-scale for HI/ H_2 formation-destruction is

$$t_{\text{eq}} = \frac{1}{D + 2Rn}, \quad (5)$$

where D is the local (attenuated) photodissociation rate. For molecular gas $D/(2Rn) \ll 1$ and $t_{\text{eq}} \simeq 1/(2Rn) \approx 5 \times 10^8/n$ yr. For atomic gas $D/(2Rn) \gg 1$ and $t_{\text{eq}} \simeq 1/D$. In free-space $D = D_0$ and $t_{\text{eq}} \approx 5.5 \times 10^2/I_{\text{UV}}$ yr.

2.3. Multiphased Gas

For a multiphased CNM/WNM mixture of HI gas in which the heating is dominated by photoelectric emission from dust grains, the field intensity I_{UV} and the density n_{CNM} of the CNM are correlated, with (Wolfire et al. 2003)

$$n_{\text{CNM}} = 22.7 I_{\text{UV}} \left(\frac{4.1}{1 + 3.1 Z_g^{0.365}} \right) \left(\frac{Z'_g}{Z'_{\text{C,O}}} \right) \left(\frac{\phi_{\text{CNM}}}{3} \right) \text{cm}^{-3}. \quad (6)$$

Here $Z'_{\text{C,O}}$ is the *gas phase* carbon-oxygen abundance relative to the abundances at solar metallicity. That is, $Z'_{\text{C,O}}$ is the “gas-phase metallicity”. In Equation (6), ϕ_{CNM} expresses the range for which the CNM can be in pressure equilibrium with the WNM. Typically, $\phi_{\text{CNM}} \sim 3$. For multiphase conditions the WNM density is $n_{\text{WNM}} \sim 0.01 n_{\text{CNM}}$, and the gas is thermally unstable (UNM) for densities between n_{WNM} and n_{CNM} (see Figure 9 of Wolfire et al. 2003).

It follows from Equations (4) and (6) that for HI-to- H_2 transitions occurring in pure CNM at thermal pressures allowing multiphase conditions (KMT, S14)

$$\alpha G = (\alpha G)_{\text{CNM}} \equiv 2.58 \left(\frac{1 + 3.1 Z_g^{0.365}}{4.1} \right) \left(\frac{Z'_{\text{C,O}}}{Z'_g} \right) \times \left(\frac{3}{\phi_{\text{CNM}}} \right) \left(\frac{2.62}{1 + (2.64\phi_g Z'_g)^{1/2}} \right) \phi_g. \quad (7)$$

In § 4 we will consider perturbations to $(\alpha G)_{\text{CNM}}$ by varying independently the parameters ϕ_g , Z'_g , and $Z'_{\text{C,O}}$, all for ϕ_{CNM} in the realistic range of 2 to 5.

3. $\Sigma_{\text{H}_2}/\Sigma_{\text{HI}}$ IN PERSEUS

Equation (1) can be reexpressed as an HI mass surface density

$$\Sigma_{\text{HI}} = 6.71 \left(\frac{1.9}{\sigma_{g-21}} \right) \ln \left[\frac{\alpha G}{3.2} + 1 \right] M_{\odot} \text{ pc}^{-2}, \quad (8)$$

where $\sigma_{g-21} = \sigma_g / (10^{-21} \text{ cm}^2)$. (In Equation (8) the contribution of helium to the mass is not included). If $\Sigma_{\text{tot}} \equiv \Sigma_{\text{HI}} + \Sigma_{\text{H}_2}$ is the total hydrogen gas surface density, and $\mathcal{R}_{\text{H}_2} \equiv \Sigma_{\text{H}_2}/\Sigma_{\text{HI}}$ is the molecular-to-atomic mass ratio, then

$$\mathcal{R}_{\text{H}_2}(\Sigma_{\text{tot}}) = \frac{\Sigma_{\text{tot}}}{\Sigma_{\text{HI}}} - 1. \quad (9)$$

For optically thick clouds, $\Sigma_{\text{HI}}(\sigma_g, \alpha G)$ (as given by Equation [8]) is independent of Σ_{H_2} , and \mathcal{R}_{H_2} varies linearly with Σ_{tot} with slope $1/\Sigma_{\text{HI}}$.

In Figure 1 we plot the L15 data for \mathcal{R}_{H_2} versus Σ_{tot} for the five dark and star-forming regions in Perseus B1, B1E, B5, IC348 and NGC1333. A complete discussion of the data extraction methodology is presented in L12/L15. For each region, each data point corresponds to a distinct sight-line through the complex. Many of the sight-lines probe substantial columns of H_2 and pass well through the HI-to- H_2 transition layers. For example, \mathcal{R}_{H_2} approaches 10 in IC348 and NGC1333.

We fit our Equation (9) to the data points using a standard weighted-least-squares procedure, and find the best-fitting total HI surface density for each region. The total HI surface mass densities lie within the narrow range of 6.3 to 9.2 $M_{\odot} \text{ pc}^{-2}$, and are listed in Table 1.

The (red) curves in Figure 1 are our best fits for \mathcal{R}_{H_2} versus Σ_{tot} as given by Equation (9) and the HI surface densities in Table 1. The theoretical curves are in excellent agreement with the data. This implies that the sight-lines are indeed probing optically thick complexes with complete HI-to- H_2 transitions.

For characteristic CNM, $\alpha G = (\alpha G)_{\text{CNM}} \approx 2.58$ as given by Equation (7). For a standard $\sigma_{g-21} = 1.9$ the HI column for pure CNM shielding is then $\Sigma_{\text{HI}}^{\text{CNM}} = 4.0 M_{\odot} \text{ pc}^{-2}$, significantly smaller than the observed total HI columns. This implies that if the entire HI columns are contributing to the shielding of the H_2 cores in Perseus, these shielding columns must be multiphased, not just CNM. Alternatively, if the shielding is assumed to be entirely CNM, not all of the observed HI contributes to the shielding. We discuss these conclusions in more detail in §4.

4. ANALYSIS

4.1. Shielding and HI Gas Densities

According to Equation (1) or (8) the total HI surface density depends on just σ_g and αG , so that curves of constant HI surface density may be drawn in the σ_g versus αG parameter space. In Figure 2 (all three panels) we plot the locus curves (in color) for the Σ_{HI} inferred for each of the five Perseus regions. As expected, for any Σ_{HI} a large αG requires a large σ_g , and vice versa.

The two horizontal dashed lines in Figure 2 represent the range of grain absorption cross sections we consider in our

analysis, from the standard $\sigma_{g-21} = 1.9$ to a larger $\sigma_{g-21} = 3.8$. We consider an enhanced σ_g because L15 found that the visual extinction per hydrogen gas column in Perseus is $A_V/N_{\text{HI}} = 1.0 \times 10^{-21} \text{ mag cm}^2$, about a factor of 2 larger than for standard Galactic extinction, and this may imply a correspondingly larger than usual dust-grain absorption cross section. A larger σ_g could be due to (a) altered dust properties at a normal dust-to-gas mass ratio, i.e. $\phi_g = 2$ and $Z'_g = 1$, or (b) typical (diffuse) ISM dust but with a higher abundance, i.e. $\phi_g = 1$ and $Z'_g = 2$. In any case, the gas-phase metallicity, $Z'_{\text{C,O}}$, appears close to Solar in Perseus (Hernández et al. 2009).

For any assumed σ_g the implied αG for each source may be read off the plots in Figure 2. In Table 2 we list the range of inferred αG parameters for each region, for $\sigma_{g-21} = 1.9$ to 3.8. The αG are large ($\gtrsim 1$) and this implies that the attenuation of the photodissociating LW radiation is in the strong-field limit with HI-to- H_2 transitions dominated by dust absorption within the outer atomic envelopes (“HI -dust”). This as opposed to HI-to- H_2 transitions controlled by H_2 -line self-shielding.

For any given αG , the effective gas densities, n , in the HI gas depends on the assumed FUV radiation intensity I_{UV} (see Eq. 4). By “effective” we mean for a uniform density medium. As discussed by L12 within most of the Perseus system, the photodissociating radiation is dominated by the background Galactic light. This is consistent with the overall thermal infrared dust emission temperatures (16 – 22 K) as well as with the anomalous microwave emissions (Tibbs et al. 2011). For FUV dust heating, $I_{\text{UV}} \approx 1$ within a factor of 2. The radiation fields near IC345 and NGC1333 may be locally enhanced by the presence of one or two B5 V-type stars.

In Table 2 we list the inferred gas densities assuming $I_{\text{UV}} = 1$, for $\sigma_{g-21} = 1.9$ and 3.8. The inferred densities scale linearly with the assumed I_{UV} . For $\sigma_{g-21} = 3.8$ the densities depend on whether (a) $\phi_g = 2$ and $Z'_g = 1$, or (b) $\phi_g = 1$ and $Z'_g = 2$. The densities are a factor-two smaller for the second option (see again Eq. 4). Overall the effective HI densities range from ~ 2 to 10 cm^{-3} . The gas densities in the H_2 cores are likely larger, enabling molecule formation on a time scales $1/(2Rn) \simeq 5 \times 10^8/n \text{ yr}$ (see Equation (5)), within the lifetime of the Perseus cloud $\sim 10 - 100 \text{ Myr}$. In the HI layers the equilibrium time-scales are $1/D \ll 1/(2Rn)$ and a photodissociation steady state is achieved.

In Table 2 we also list the range of length scales, $\ell \equiv N_{\text{HI}}/n$, for the atomic shielding envelopes given the observed HI columns. With exception of NGC 1333 (which may be influenced by a B5V star) the derived length scales are comparable, and within factors 2-3, with the overall $\sim 80 \text{ pc}$ HI kinematic size scale of the Perseus complex. The inferred sizes are perhaps too large for “option-b” ($Z'_g = 2$, $\phi_g = 1$) and more consistent with “option-a” ($Z'_g = 1$, $\phi_g = 2$) for which a larger dust cross section reflects an intrinsic variation in grain properties.

4.2. Is the HI Multiphased?

The gas densities that we have inferred above are lower than the densities expected for pure CNM as given by Equation (6), and are intermediate between n_{CNM} and n_{WNM} . This suggests that the observed HI columns are multiphased mixtures. If most of the HI extends to just the kinematic diameter of $\sim 80 \text{ pc}$ (Imara & Blitz 2011) much of the HI must be thermally

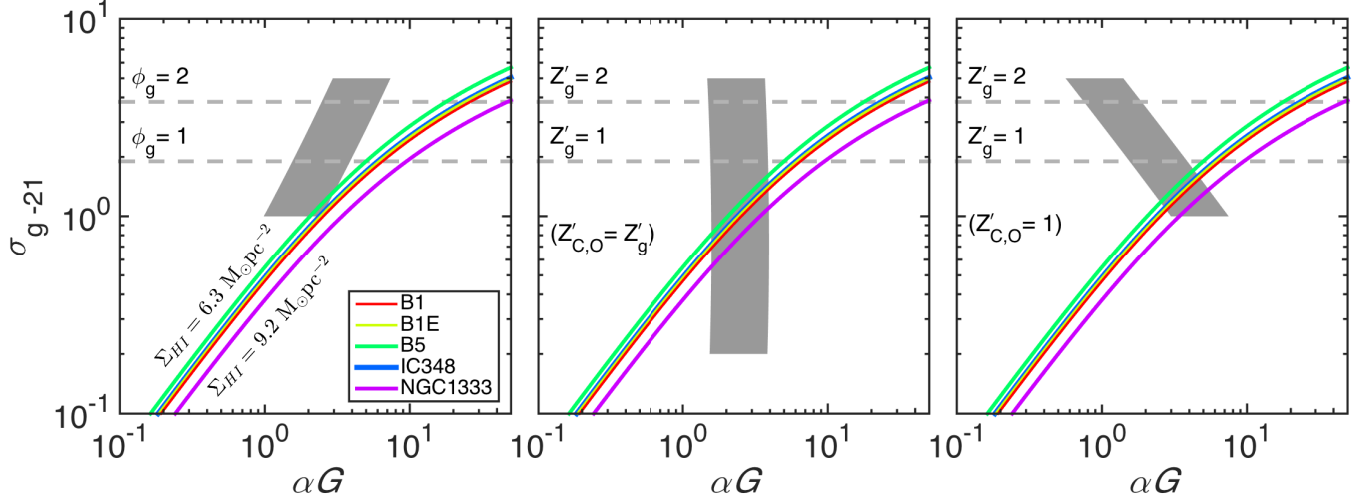


FIG. 2.— The observed HI contours in the $\sigma_g - \alpha G$ parameter space. The horizontal dashed lines are for $\sigma_{g-21} = 1.9$ and 3.8 . The grey strips are where $\alpha G = (\alpha G)_{\text{CNM}}$ (Equation [7]) for ϕ_{CNM} in the range $2 - 5$, (with ϕ_{CNM} increasing from right to left across the strip). The dust cross section $\sigma_{g-21} = 1.9\phi_g Z'_g$ varies with the dust abundance Z'_g and the intrinsic dust absorption properties ϕ_g . The left panel is for variations in ϕ_g assuming $Z'_g = Z'_{\text{C,O}} = 1$. The middle and right panels are for variations in Z'_g with $\phi_g = 1$, assuming $Z'_{\text{C,O}} = Z'_g$ (middle) or $Z'_{\text{C,O}} = 1$ (right), see §4 for details.

TABLE 2
 αG , VOLUME DENSITY RANGES, AND LENGTH SCALES, FOR σ_{g-21} IN THE RANGE $1.9 - 3.8$ FOR $I_{\text{UV}} = 1$.

Source	αG	$\phi_g = 1 - 2$ with $Z'_g = 1$		$Z'_g = 1 - 2$ with $\phi_g = 1$	
		n (cm^{-3})	Length Scale (pc)	n (cm^{-3})	Length Scale (pc)
B1	6.5 – 26.1	9.1 – 3.6	33 – 84	9.1 – 1.8	33 – 169
B1E	6.1 – 23.8	9.6 – 3.9	30 – 74	9.6 – 2.0	30 – 149
B5	5.0 – 17.7	11.8 – 5.3	22 – 49	11.8 – 2.6	22 – 97
IC345	6.0 – 23.2	9.8 – 4.0	30 – 72	9.8 – 2.0	30 – 144
NGC1333	9.5 – 47.0	6.2 – 2.0	61 – 189	6.2 – 1.0	61 – 379

unstable, possibly in a cooling transition from the WNM to CNM phases.

These conclusions are also indicated by the positions of the grey strips in Figure 2. The strips show the regions in the parameter space for which $\alpha G = (\alpha G)_{\text{CNM}}$ for different (realistic) perturbations of the controlling quantities in Equation (7). In the left-hand panel the grey strip is for variations in ϕ_g from 0.5 to 3 assuming $Z'_g = Z'_{\text{C,O}} = 1$. The middle panel is for metallicities between 0.1 and 3 assuming $Z'_g = Z'_{\text{C,O}}$ and with $\phi_g = 1$. The grey strip in the right-hand panel is for variations in just Z'_g from 0.5 to 3 , but with $Z'_{\text{C,O}} = 1$ and again $\phi_g = 1$. The width of each strip corresponds to the range $2 \leq \phi_{\text{CNM}} \leq 5$, for CNM at multiphased conditions, with ϕ_{CNM} increasing from right to left across the strips.

It is evident from Figure 2 that for σ_{g-21} between 1.9 and 3.8 , the contours for the observed HI column densities are to the right of the grey strips, with αG always significantly greater than $(\alpha G)_{\text{CNM}}$ (i.e., $n < n_{\text{CNM}}$) for all types of perturbations in the parameters ϕ_g , Z'_g and $Z'_{\text{C,O}}$ shown in the three panels. This implies that the HI cannot consist of pure CNM gas. For the HI to be fully CNM, the dust absorption cross section would have to be lower than expected, e.g. if the metallicity were reduced (see middle panel).

Importantly, our conclusion that the HI cannot be pure CNM depends on the inclusion of the denominator $w \equiv 1/[1 + (2.64\phi_g Z'_g)^{1/2}]$ in Equation (4). As discussed by S14, w accounts for the reduction of the effective dissociation bandwidth by H_2 -dust. (This factor is not included in the KMT

approximations.) For example, $w = 0.4$ for $\sigma_{g-21} = 1.9$ with $\phi_g = 1$ and $Z'_g = 1$. Excluding w in Equation (4) would shift the “CNM strips” to the right in Figure 2 much closer to the HI contours. Without the H_2 -dust absorption term the inferred effective HI volume densities would be more than twice larger than listed in Table 2, and much closer to n_{CNM} as given by Equation (6) for $I_{\text{UV}} = 1$.

5. DISCUSSION AND SUMMARY

L12/L15 used the “spherical cloud” model developed by KMT (and updated by McKee & Krumholz 2010) to analyze the HI-to- H_2 transitions in the various Perseus regions (e.g., see Fig. 11 in L15). In their analysis, each region consists of many individual spheres with H_2 cores surrounded by HI shells, and each sight-line probes the area-averaged mass ratios $\mathcal{R}_{\text{H}_2} \equiv \langle \Sigma_{\text{H}_2} \rangle / \langle \Sigma_{\text{HI}} \rangle$ as functions of $\langle \Sigma_{\text{tot}} \rangle$ for each sphere. Furthermore, L12/L15 adopted the KMT ansatz that the HI shielding envelopes are dominated by CNM, and then estimated ϕ_{CNM} for each region assuming $n = n_{\text{CNM}}$.

As discussed in detail by S14 the differences in the predicted HI columns and H_2 mass fractions for individual clouds are very small for plane-parallel versus spherical geometries. However, the χ_{KMT} parameter differs from the S14 αG (see also Sternberg 1988), since it does not include the H_2 -dust absorption factor $w \equiv 1/[1 + (2.64\phi_g Z'_g)^{1/2}]$. For a given αG (Equation [4]) and an assumed I_{UV} the implied gas density n is increased if w is excluded. Thus, including the H_2 -dust term in αG is essential for determining how close the gas density is to the CNM density for multiphased conditions.

In their analysis, L12/L15 assumed that $Z'_g = Z'_{C,O} = 1$. They also set $\sigma_{g-21} = 1.0$ corresponding to $\phi_g = 1/1.9$ in our Equation (2). It is evident from the left-hand panel of our Figure 2 that for $\sigma_{g-21} = 1.0$, the contours for the observed HI columns imply αG of 2.0 to 3.4, and are to the right of the grey CNM strip. Enforcing CNM for the HI would then require $\phi_{\text{CNM}} \lesssim 2$. L12/L15 derived larger ϕ_{CNM} ($\sim 5 - 10$) for the various regions because the H_2 -dust term w is not included in the χ_{KMT} they used. Without this factor the grey CNM strips in Figure 2 are shifted to the right. For $\sigma_{g-21} = 1.0$ the inferred ϕ_{CNM} factors are then increased to the larger values found by L12/L15.

In our analysis, we do not assume *a priori* that $\alpha G = (\alpha G)_{\text{CNM}}$, instead we infer the effective HI gas densities. Our inferred densities range from ~ 2 to 10 cm^{-3} depending on the precise FUV intensity in Perseus, and on the assumed metallicities and FUV grain absorption cross section. These densities suggest that the HI shielding envelopes in Perseus are likely multiphased mixtures. If most of the HI is limited to the kinematic 21 cm radius and shields the H_2 cores, then a significant fraction must be thermally unstable. Alternatively some of the HI could be very extended WNM and

not associated with the shielding. This follows from just our radiative transfer analysis of the HI-to- H_2 transitions and HI columns using our Equation (1). The behavior in Perseus suggests that in addition to CNM, less dense UNM and perhaps some diffuse WNM, are important in controlling the global HI-to- H_2 transitions and Schmidt-Kennicutt thresholds in external galaxies, from low- to high-redshifts (Leroy et al. 2008; Tacconi et al. 2010; Bolatto et al. 2011; Schrubba et al. 2011; Genzel et al. 2013).

We thank B.-G. Andersson, A. Goodman and C. F. McKee for helpful conversations about the Perseus cloud. S.B. acknowledges support from the Raymond and Beverly Sackler Tel Aviv University – Harvard/ITC Astronomy Program. M.-Y. L acknowledges supports from the DIM ACAV. This work was also supported in part by the DFG via German – Israeli Project Cooperation grant STE1869/1-1/GE625/15-1, by the PBC Israel Science Foundation I-CORE Program grant 1829/12, by the grant SYMPATICO (ANR-11-BS56-0023) from the French Agence Nationale de la Recherche, and by the French CNRS national program PCMI.

REFERENCES

- Bachiller, R., & Cernicharo, J. 1986, AA, 166, 283
 Bally, J., Walawender, J., Johnstone, D., Kirk, H., & Goodman, A. 2008, Handb. Star Form. Reg., 4
 Bolatto, A. D., Leroy, A. K., Jameson, K., et al. 2011, ApJ, 741, 12
 Draine, B. T. 1978, ApJS, 36, 595
 Genzel, R., Tacconi, L. J., Kurk, J., et al. 2013, ApJ, 773, 68
 Hernández, J. I. G., Iglesias-Groth, S., Rebolo, R., et al. 2009, ApJ, 706, 866
 Imara, N., & Blitz, L. 2011, ApJ, 732, 78
 Kirk, H., Johnstone, D., & Di Francesco, J. 2006, ApJ, 646, 1009
 Krumholz, M. R., McKee, C. F., & Tumlinson, J. 2009, ApJ, 693, 216
 Lee, M.-Y., Stanimirovic, S., Murray, C. E., Heiles, C., & Miller, J. 2015, ApJ in press, arXiv:1504.07405
 Lee, M.-Y., Stanimirović, S., Douglas, K. A., et al. 2012, ApJ, 748, 75
 Leroy, A. K., Walter, F., Brinks, E., et al. 2008, AJ, 136, 2782
 McKee, C. F., & Krumholz, M. R. 2010, ApJ, 709, 308
 Miville-Deschênes, M.-A., & Lagache, G. 2005, ApJS, 157, 302
 Peek, J. E. G., Heiles, C., Douglas, K. A., et al. 2011, ApJS, 194, 20
 Ridge, N. A., Di Francesco, J., Kirk, H., et al. 2006, Astron. J., 131, 2921
 Sancisi, R., Goss, W. M., Anderson, C., Johansson, L. E. B., & Winnberg, A. 1974, AA, 35, 445
 Sargent, A. I. 1979, ApJ, 233, 163
 Schrubba, A., Leroy, A. K., Walter, F., et al. 2011, AJ, 142, 37
 Sternberg, A. 1988, ApJ, 332, 400
 Sternberg, A., Petit, F. L., Roueff, E., & Bourlot, J. L. 2014, ApJS, 790, 10S
 Tacconi, L. J., Genzel, R., Neri, R., et al. 2010, Nature, 463, 781
 Tibbs, C. T., Flagey, N., Paladini, R., et al. 2011, MNRAS, 418, 1889
 Ungerechts, H., & Thaddeus, P. 1987, ApJS, 63, 645
 Wolfire, M. G., McKee, C. F., Hollenbach, D., & Tielens, A. G. G. M. 2003, ApJ, 587, 278